

Optical fibre taper-enabled waveguide photoactuators

Jianliang Xiao

Zhejiang Lab

Tao Zhou

Institute of Flexible Electronics Technology of THU, Zhejiang

Ni Yao

Zhejiang Lab

Shuqi Ma

Zhejiang Lab

Chenxinyu Pan

Zhejiang University

Pan Wang (✉ nanopan@zju.edu.cn)

Zhejiang University <https://orcid.org/0000-0003-4209-5186>

Haoran Fu

Institute of Flexible Electronics Technology of THU, Zhejiang

Haitao Liu

Zhejiang Lab <https://orcid.org/0000-0003-1824-0304>

Jing Pan

Zhejiang University

Longteng Yu

Zhejiang Lab

Shipeng Wang

Zhejiang Lab

Wenzhen Yang

Zhejiang Lab

Limin Tong

Zhejiang University

Lei Zhang

Zhejiang University <https://orcid.org/0000-0002-0826-169X>

Article

Keywords:

Posted Date: July 12th, 2021

DOI: <https://doi.org/10.21203/rs.3.rs-657262/v1>

License:  This work is licensed under a Creative Commons Attribution 4.0 International License.

[Read Full License](#)

Version of Record: A version of this preprint was published at Nature Communications on January 18th, 2022. See the published version at <https://doi.org/10.1038/s41467-022-28021-4>.

Abstract

Photoactuators have attracted tremendous interest yet most of them rely on free-space illumination, which requires a line-of-site low-loss optical path. While waveguide photoactuators can overcome this limitation, their actuating performances are fundamentally restricted by the nature of standard optical fibres. Herein, we demonstrated miniature photoactuators by embedding optical fibre taper (OFT) in a polydimethylsiloxane/Au nanorod-graphene oxide photothermal film. The special geometric features of OFT endow the OFT photoactuator (OPA) with microscale active layer thickness, high energy density and optical coupling efficiency. Hence, OPAs show large bending angles ($> 270^\circ$), fast response (1.8 s for 180° bending), and low energy consumption ($< 0.55 \text{ mW}/^\circ$), significantly exceeding the performance of state-of-the-art waveguide photoactuators. As a proof-of-concept study, biomimetic chameleon tail and tongue are realized. A two-arm soft gripper is further demonstrated for capturing/moving small objects, which is challenging for free-space light-driven photoactuators. This study hopes to pave the way toward a new category of photoactuators.

Introduction

Soft actuators, which are capable of converting external stimuli to the desired shape changes or mechanical movements, can provide safe, comfortable and flexible human-machine interaction¹, and hold great potential in many cutting-edge applications, such as soft robots²⁻⁵, artificial muscles⁶⁻⁸, biomimetic propellers⁹⁻¹² and soft grippers¹³⁻¹⁵. Various soft actuators driven by different stimuli including magnetic fields^{16,17}, electric fields^{1,18,19}, temperature^{20,21}, humidity^{15,22} and light have been widely reported. Among them, light-driven actuators, *i.e.* photoactuators, have attracted particular research interest due to the advantages of light, such as immunity of electromagnetic interference, safe operation in explosive atmosphere and flexible tunability in wavelengths, intensity and polarization²³⁻²⁷.

To date, most photoactuators are triggered by free-space illumination, which requires a line-of-site low-loss optical path between the light source and the actuator²⁸⁻³⁰. As such, the utility of these photoactuators is vitally restricted in cases where direct and constant line-of-site access is absent. Besides, the intensity of free-space light may decrease significantly during long-distance transport, especially for the environment with strong absorption and scattering^{9,13}. Moreover, for the free-space light-driven actuators to execute locomotion or handle objects, the control light generally needs to intentionally follow the motion of the actuator¹, which vastly restricts the maneuverability and convenience. Alternatively, optical fibres provide an efficient strategy to guide light into actuators to overcome these limitations, since light can be transmitted over long distances with low optical loss through flexible and bendable optical fibres³¹. Recently, a few optical fibre-enabled photoactuators have been reported by taking advantages of waveguided light³¹⁻³³. For example, Zhou et al. reported a poly(N-isopropylacrylamide) waveguide photothermal actuator, which employed a plastic optical fibre to guide 532-nm-wavelength laser. For this photoactuator, the bending angle was less than 60° and the response time was over 50 s³². Kuenstler et al. demonstrated a waveguide photoactuator made of liquid crystal

elastomer, achieving a bending angle of 15° and response time of longer than 5 s^{31} . These reports shed light on the development of waveguide photoactuators, however, all of them suffered from limited bending amplitude and long response time. This could be ascribed to three possible reasons: (1) large thickness of the active layer due to the relatively large size of the commercially available optical fibre (typically $> 100\ \mu\text{m}$ in diameter); (2) low energy density due to the non-focused light beam; (3) low optical coupling efficiency due to the size mismatch between the optical waveguide and the photo-responsive material. To address these issues, a thinner optical fibre with enhanced optical intensity is highly desired for high-performance photoactuators with large deformation and fast response.

Optical fibre tapers (OFTs), which are taper-drawn from standard optical fibres^{34,35} and have a tip diameter less than $1\ \mu\text{m}$, are capable of guiding light with tailorable optical confinement and low optical loss (e.g., $< 0.05\ \text{dB/cm}^{36}$, much lower than any other optical waveguides of similar sizes). Therefore, the small size of OFT makes it possible to reduce the thickness of active layer and overcome the size mismatch between optical waveguide and photo-responsive material. More importantly, the energy density of light guided by OFT is much higher than that of commercially available optical fibres, resulting in a higher photothermal conversion efficiency.

Herein, we propose an OFT photoactuator (OPA) that can drive large deformation, in which OFT is used as a key component to guide light into the photothermal film (Fig. 1a). Benefiting from the special geometric features of OFT, *i.e.* micro/nanoscale diameter and long taper region, the OPA features a thin active layer, high energy density and optical coupling efficiency, which enable much larger bending angle ($> 270^\circ$) than waveguide actuators reported before, high actuation efficiency and low energy consumption ($< 0.55\ \text{mW}/^\circ$). In addition, the OPA demonstrates excellent stability, controllability and maneuverability during repeated actuation, which is particularly valuable for the accurate control when executing a task that requires dynamic location. As an example, we show that a one-arm OPA can imitate the functions of the tail and tongue of chameleons during predation, and a two-arm OPA soft gripper can capture, move and release objects with different shapes, which is challenging for free-space light-driven actuators. We believe that OPA will pave a new way to design easy-to-maneuver photoactuators with large deformation.

Results

Fabrication of OPAs. As shown in Fig. 1a, an OPA is composed of a photo-responsive elastomeric composite sheet with an OFT embedded in the middle as the waveguide. The elastomeric composite sheet is made of a polydimethylsiloxane (PDMS) film, which is doped with Au nanorods (AuNRs) as the photothermal agent, and a graphene oxide (GO) film. When a control light is launched into the elastomeric composite via the OFT, photothermal heating induced by the AuNR will cause a significant expansion of the PDMS/AuNR layer due to the high coefficient of thermal expansion (CTE) of PDMS^{37,38}. On the other hand, GO layer undergoes negligible thermal expansion due to its low CTE. Thus, the mismatch between the CTE and deformations of two layers leads to a dramatic bending of the OPA. When the light is switched off, the OPA recovers back to its initiate state. Figure 1b shows a detailed preparation process of the OPA. Firstly, a thin layer of PDMS doped with AuNRs was spin-coated onto a

glass substrate as the first layer of the elastomeric composite sheet. Then, an array of OFTs were embedded in the PDMS layer with an interval of ~ 5 mm, which were subsequently covered with a thin layer of GO sheet. Finally, as fabricated photo-responsive elastomeric composite sheet was cut into small pieces to obtain OPAs. AuNRs used in OPAs, with average length and diameter of ~ 51 and 23 nm respectively (Fig. 1c, left inset), show an ensemble longitudinal surface plasmon resonance peak around 638 nm (Supplementary Fig. 1), which matches well with the peak wavelength of the control light. Due to the high absorption cross section (Fig. 1c) and strong local-field enhancement (Fig. 1c, right inset), the AuNRs can efficiently generate heat in the PDMS layer via the nonradiative decay of LSPR excited by the control light. OFTs were fabricated by flame-heated taper drawing^{34,35} of standard optical fibres. Figure 1d shows an optical microscope of a typical OFT with a taper length of ~ 1.75 cm and a tip diameter of ~ 700 nm. The relatively long taper can effectively suppress the intermodal energy transfer in the taper region and satisfy the adiabatic condition^{34,39}, guaranteeing the high optical coupling efficiency, while the small tip diameter is advantageous for the seamless shrink of beam size down to micrometer scale. The cross-sectional view of an as-fabricated elastomeric is shown in Fig. 1e, in which a layer of PDMS/AuNR with a thickness of ~ 70 μm and a layer of GO with a thickness of ~ 1.5 μm can be clearly seen. Despite of the thin thickness, the GO layer shows a fine lamellar structure and typical wrinkled surface, benefiting from the outstanding self-assembly ability of GO sheets with large lateral dimension (Supplementary Fig. 2). When guiding a 635 -nm-wavelength laser into an OPA, a clear light propagation path in the sheet can be observed due to the scattering of light by the AuNRs (Fig. 1f). The width of the OPA in Fig. 1f was designedly broadened to completely display the light propagation path, while the typical size of OPA is usually ~ 500 μm in width and ~ 1 cm in free length (Fig. 1g and Supplementary Fig. 3).

Light-driven actuation. As previously mentioned, the actuation mechanism of OPA is based on the CTE mismatch and asymmetric deformation of the PDMS/AuNR-GO bilayer under photothermal heating. We first investigated the deformation behavior of an OPA when a temperature rise is directly applied onto the bilayer structure. As shown in Fig. 2a, the PDMS/GO bilayer (70 $\mu\text{m}/1.5$ μm) undergoes a reversible bending when the environmental temperature is switched between room temperature (RT, 20 $^{\circ}\text{C}$) and 60 $^{\circ}\text{C}$, which is simulated based on finite element analysis (FEA, see details in Methods). The simulated bending angle of the OPA increases linearly with the increase of environmental temperature (Fig. 2b and Supplementary Fig. 4), which agrees very well with the experimental results by putting it on a hot plate. Thus, by taking advantage of the photothermal effects of embedded AuNRs, OPA can undergo similar bending. As shown in Fig. 2c, when a 635 -nm-wavelength laser (75 mW) was launched into the OPA, the temperature rise induced by the photothermal effect leads to a significant bending of OPA, with the highest temperature (T_{max}) of ~ 110 $^{\circ}\text{C}$ located near the OFT tip of the OPA. It is worth to note that there is a diminishing bending curvature along the longitudinal direction due to the gradient distribution of temperature. Figure 2d compares laser power-dependent T_{max} of OPAs fabricated with different components. As expected, the AuNR plays an important role in the light-to-heat conversion of the OPA, and the GO also shows notable conversion ability due to its light adsorption property in the UV-Vis spectral range (Supplementary Fig. 5). The T_{max} of an OPA composed of PDMS/AuNR-GO under 150 mW

laser is as high as 170 °C, which is benefited from the significantly enhanced energy density near the OFT tip and the high photothermal conversion efficiency of AuNRs.

The light-driven deformation amplitude of OPAs can be readily regulated by controlling the laser power. With the increase of control laser power, the bending angle increases gradually (Fig. 3a and Supplementary Fig. 6). The highest bending angle is larger than 270° at 150 mW, which is much larger than the bending angle (< 60°) of other types of waveguide actuators^{31–33}. In addition, the bending angle of OPA is also much larger than that of the actuator driven by free-space light under the same laser power of 150 mW (Fig. 3b, I). When illuminated with a free-space laser beam, the PDMS/AuNR-GO film can only absorb a small portion of the light, while the rest is wasted since the illuminating area is larger than the film. As a result, the energy efficiency is pretty low and the bending angle is only 62°. Using OFT to guide light into the PDMS/AuNR-GO film can effectively overcome this problem since the light can be guided along the film and absorbed continuously, allowing for a higher energy efficiency and larger bending angle. The energy consumption to drive the OPA is as low as < 0.55 mW/°, indicating the high actuation efficiency with the use of OFT, which is favorable for the cost-cutting and miniaturization of the integrated device in practical applications.

On the other hand, the small tip diameter of the OFT (Fig. 1d) allows for reducing the thickness of OPA to less than 100 µm, which is favorable for large bending angles. In contrast, the actuator fabricated with a standard optical fibre has a total thickness of ~ 220 µm due to the large diameter of the standard optical fibre (Supplementary Fig. 7a, b), and the bending angle under 150-mW laser is only 56° (Fig. 3b, II). The detailed influences of thicknesses of each layer on the bending angles of OPA are shown in Supplementary Fig. 8. In addition, OPA with similar thickness (~ 225 µm, Supplementary Fig. 7c) also shows larger bending angle (85°) than that of standard optical fibre-based actuator (Fig. 3b, III), which indicates that the enhanced energy density, produced by the small tip diameter of the OFT, also favors the efficient actuation of the OPA. In summary, the thickness as thin as 70 µm, along with the improved energy density and optical coupling efficiency, endow the OPA with excellent light-driven actuating performances.

Dynamic deformation of the OPA under 120 mW laser indicates a rapid response of the OPA (Fig. 3c and Supplementary Movie 1). It takes only 1.8 s to reach a bending angle greater than 180° (~ 70% of the total deformation), whereas the recovery of the 70% bending takes 2.3 s after the switch off of the laser. This is understandable because the cooling process of PDMS is slower than the heating process. The fast response of OPAs is probably ascribed to the high energy density and thin thickness of active layer benefiting from the small tip of OPT. Moreover, the OPA shows negligible decay in deformation after more than 3000 actuations with a standard deviation of 3.62° and coefficient of variation as low as 0.14 (Fig. 3d and Supplementary Fig. 9). The excellent stability and maneuverability endow OPAs with significant advantages in accurate control when executing a task that involves location changes, while the free-space light-driven actuators suffer from the difficulties in accurately controlling the illuminating spot.

Biomimetic applications. Many natural activities of creatures can be regarded as a series of actuations performed through various actuators with different functions. For example, when a chameleon on a branch preys an insect, its tail winds the branch to keep balance (function i), and its tongue reaches out and captures the insect (function ii), as shown in Fig. 4a. Inspired by this, an OPA is used to mimic the predation of chameleons. As shown in Fig. 4b, the OPA winds rapidly onto a plastic pipe under 635-nm laser within 2.2 s (panels 1–3), and unwinds gradually after switching the control laser off (panels 4–6), which clearly imitates the function of the tail (see more details in Supplementary Movie 2). Similarly, the OPA can grasp an ant (~ 20 mg) stayed on a tip immediately with the switch on of control laser (Fig. 4c and Supplementary Movie 3), which imitates the function of the tongue. Benefiting from the large bending deformation, the OPA can hold the ant firmly and take it off from the tip, showing great potential in biomimetic target capture.

In fact, target capturing/moving is an important and challenging application of photoactuators. For the use of free-space light-driven actuators to capture/move objects, the illuminating spot needs to be accurately controlled to follow the moving of actuators or a large illuminating beam covering the whole operating area should be supplied, which greatly restricts the maneuverability and operating area. However, for OPAs demonstrated here, they are seamlessly connected to optical fibres, allowing the control light to intrinsically follow the moving of actuators. Thus, OPAs hold significant advantages in accurately handling and moving objects in a wide operating area. A soft gripper composed of two OPA strips was fabricated to capture objects with different shapes (Fig. 5 and Supplementary Movie 4–6). Initially, the two OPA strips bend outwards with the GO sides aligned face to face to offer an opening angle large enough for accommodating different objects with complex shapes. With the switch on of 635-nm laser, the two arms of the OPA gripper bend inwards to capture and lift targets such as a cuboid, a ball and three balls, as shown in Fig. 5. When the laser is switched off, the gripper arms bend reversely to release the object. Alternatively, the OPA strips can also initially form an inward bending configuration for the gripper to capture small objects (Supplementary Fig. 10 and Supplementary Movie 7, 8).

Discussion

In summary, we have demonstrated miniature waveguide photoactuators (*i.e.* OPAs) using OFT to guide the control light, which are free from the restrictions of free-space light. The special geometric features of the OFT endow the OPA with much enhanced actuating performances, overcoming the main challenges to develop waveguide photoactuators with large bending amplitude, and thus paving a new way to design photoactuators driven by waveguided light. Differently from the free-space light-driven actuators which suffer from the difficulties in accurately controlling the illuminating spot, the light supply of OPA is located inside the material and controlled in real time, which gives OPAs significant advantages in executing tasks involving location changes, such as handling and moving objects with different shapes. The more complex deformation of OPAs can be readily achieved by regulating the transport and absorption of light in it and more potential applications, such as searching in unstructured environment, deepwater sampling, and in vivo diagnosis/therapy, can be realized by the special designs of the deformation behaviors and the implementation of advanced materials.

Methods

Fabrication of OPA strips and grippers. AuNRs were prepared and modified with polyethylene glycol (PEG) according to the procedure described previously by Wang et al.⁴⁰. Then the as-prepared PEGylated AuNRs dispersed in ethanol were mixed with PDMS prepolymer component A (5 g, SYLGARD 184, DOW) before adding the component B (0.5 g). Then the degassed PDMS/AuNR prepolymer was spin-coated on a glass substrate pretreated with plasma, followed by curing at 80°C for 30 min. OFTs were fabricated from standard optical fibres (MMF 62.5/125, Corning) based on the flame brushing method^{34,35,41,42}. Briefly, a standard optical fibre was heated by an acetylene flame with a flame width of 5 mm and pulled up to break with a relative high velocity of 150–300 mm/s. The taper length and tip diameter of OFT could be modulated by controlling the pulling velocity. The obtained OFTs were then fixed on the as-prepared PDMS film, on which the PDMS/AuNR prepolymer was casting, and two strips of polyimide tape were used as spacers to control the thickness of PDMS films. After curing at 80°C for 30 min, PDMS/AuNR films with OFTs embedded in were peeled off from the substrate and treated with plasma to improve the hydrophilicity, followed by coating of GO suspensions (3 mg/mL, GaoxiTech.). The sample was then dried at 50°C and cut into individual strips containing single OFT, getting OPA strips. Due to the internal stress introduced during curing, the PDMS film showed a pre-bending after peeling off from the substrate, while the bending angle depended on the thickness and heating conditions. The pre-bending direction of obtained OPA strip could be adjusted by choosing the side to coat GO. The thickness of PDMS and GO layer in an OPA strip was regulated by the speed of spin-coating, thickness of polyimide tape spacer, and the volume of GO suspension. For the fabrication of OPA grippers, two OPA grippers were face-to-face attached on a cuboid with a gap of 1 cm and free-standing length of 1.5 cm.

Characterization and measurements. The morphology of an OPA was characterized by optical microscope (Nikon, LV150N) and field-emission scanning electron microscopy (SEM, S4800, Hitachi). UV-Vis absorption spectra were measured on a UV-Vis spectrophotometer (CARY100, Varian). The temperature of an OPA under different laser powers was measured by an infrared camera (T8, Dali Tech.). Simulated light transport in OFT was performed using Rsoft BeamPROP.

Actuation analysis of the OPA. The actuation behaviors of the OPA strips and grippers were captured by a digital video camera. The bending angles were calculated based on the method demonstrated in Supplementary Fig. 11. Thermal actuation was measured using a temperature-programmed heating plate. Light-driven actuation was achieved using a laser (OX-6351, Oxlasers) with wavelength of 635 nm and maximum power of 1 W.

FEA simulations. The commercial finite-element analysis software ABAQUS was used for the stress analysis of thermal actuation, employing the Abaqus/General solver. The thicknesses of PDMS (Young's modulus 1 MPa, Poisson's ratio 0.48, thermal expansion $300 \times 10^{-6} \text{ K}^{-1}$) layer and GO (Young's modulus 30 GPa, Poisson's ratio 0.1, thermal expansion $0.85 \times 10^{-6} \text{ K}^{-1}$) layer were 70 μm and 1.5 μm , respectively. The predefined field of temperature was applied to fulfill the computation of thermal deformation from 20 °C to 85 °C.

Declarations

Competing interests

The authors declare no competing interests.

Author Contributions

J.X. and L.Z. conceived and designed the experiments; J.X., T.Z., N.Y., S.M., C.P., P.W., H.F., H.L., J.P., L.Y., and S.W. performed the experiments and analyzed the data; T.Z. and H.F. provided guidance relating to FEA; W.Y. and L.T. provided guidance relating to data analysis and interpretation; J.X. P.W. and L.Z. wrote the manuscript; L.Z. provided overall guidance of the project. All authors read and approved the manuscript.

Acknowledgements

This work was supported by the National Natural Science Foundation of China (No. 61975173, 12004333, 62075195), the Major Scientific Research Project of Zhejiang Lab (No. 2019MC0AD01), the Key Research and Development Project of Zhejiang Province (No. 2021C05003), the Major Scientific Research Project of Zhejiang Lab (No. 2019MC0AD01), the China Postdoctoral Science Foundation funded project (No. 2020M681957), and the Zhejiang Provincial Natural Science Foundation of China (No. LQ20E030009).

Data availability

The data that support the findings within this study are available from the corresponding author upon reasonable request

References

1. Xiao, Y. Y., Jiang, Z. C., Tong, X. & Zhao, Y. Biomimetic locomotion of electrically powered "Janus" soft robots using a liquid crystal polymer. *Adv. Mater.* **31**, 1903452 (2019).
2. Hu, W., Lum, G. Z., Mastrangeli, M. & Sitti, M. Small-scale soft-bodied robot with multimodal locomotion. *Nature* **554**, 81–85 (2018).
3. Gu, G., Zou, J., Zhao, R., Zhao, X. & Zhu, X. Soft wall-climbing robots. *Sci. Robot.* **3**, eaat2874 (2018).
4. Rich, S. I., Wood, R. J. & Majidi, C. Untethered soft robotics. *Nat. Electron.* **1**, 102–112 (2018).
5. Palagi, S. & Fischer, P. Bioinspired microrobots. *Nat. Rev. Mater.* **3**, 113–124 (2018).
6. Han, B. *et al.* Plasmonic-assisted graphene oxide artificial muscles. *Adv. Mater.* **31**, e1806386 (2019).
7. Matsuda, T., Kawakami, R., Namba, R., Nakajima, T. & Gong, J. P. Mechanoresponsive self-growing hydrogels inspired by muscle training. *Science* **363**, 504–508 (2019).
8. Zhu, Q. L. *et al.* Light-steered locomotion of muscle-like hydrogel by self-coordinated shape change and friction modulation. *Nat. Commun.* **11**, 5166 (2020).

9. Shahsavan, H. *et al.* Bioinspired underwater locomotion of light-driven liquid crystal gels. *Proc. Natl. Acad. Sci. U.S.A.* **117**, 5125–5133 (2020).
10. Li, M. T., Wang, X., Dong, B. & Sitti, M. In-air fast response and high speed jumping and rolling of a light-driven hydrogel actuator. *Nat. Commun.* **11**, 10 (2020).
11. Fan, W. *et al.* Dual-gradient enabled ultrafast biomimetic snapping of hydrogel materials. *Sci. Adv.* **5**, eaav7174 (2019).
12. Zeng, H. *et al.* Light-fuelled freestyle self-oscillators. *Nat. Commun.* **10**, 9 (2019).
13. Pilz da Cunha, M., Kandail, H. S., den Toonder, J. M. J. & Schenning, A. P. H. J. An artificial aquatic polyp that wirelessly attracts, grasps, and releases objects. *Proc. Natl. Acad. Sci. U.S.A.* **117**, 2004748 (2020).
14. Wani, O. M., Zeng, H. & Priimagi, A. A light-driven artificial flytrap. *Nat. Commun.* **8**, 15546 (2017).
15. Dong, Y. *et al.* Multi-stimuli-responsive programmable biomimetic actuator. *Nat. Commun.* **10**, 10 (2019).
16. Alapan, Y., Karacakol, A. C., Guzelhan, S. N., Isik, I. & Sitti, M. Reprogrammable shape morphing of magnetic soft machines. *Sci. Adv.* **6**, eabc6414 (2020).
17. Deng, H. *et al.* Laser reprogramming magnetic anisotropy in soft composites for reconfigurable 3D shaping. *Nat. Commun.* **11**, 6325 (2020).
18. Leroy, E., Hinchet, R. & Shea, H. Multimode hydraulically amplified electrostatic actuators for wearable haptics. *Adv. Mater.* **32**, 2002564 (2020).
19. Ji, X. *et al.* An autonomous untethered fast soft robotic insect driven by low-voltage dielectric elastomer actuators. *Sci. Robot.* **4**, aaz6451 (2019).
20. Downs, F. G. *et al.* Multi-responsive hydrogel structures from patterned droplet networks. *Nat. Chem.* **12**, 363–371 (2020).
21. Jin, B. *et al.* Programming a crystalline shape memory polymer network with thermo- and photo-reversible bonds toward a single-component soft robot. *Sci. Adv.* **4**, eaao3865 (2018).
22. Zhang, Y. L. *et al.* A "Yin"- "Yang" complementarity strategy for design and fabrication of dual-responsive bimorph actuators. *Nano Energy* **68**, 8 (2020).
23. Li, J., Zhou, X. & Liu, Z. Recent advances in photoactuators and their applications in intelligent bionic movements. *Adv. Opt. Mater.* **8**, 2000886 (2020).
24. Li, Y., Liu, Y. & Luo, D. Polarization dependent light-driven liquid crystal elastomer actuators based on photothermal effect. *Adv. Opt. Mater.* **9**, 2001861 (2020).
25. Gelebart, A. H. *et al.* Making waves in a photoactive polymer film. *Nature* **546**, 632–636 (2017).
26. Ge, F., Yang, R., Tong, X., Camerel, F. & Zhao, Y. A Multifunctional dye-doped liquid crystal polymer actuator: light-guided transportation, turning in locomotion, and autonomous motion. *Angew. Chem., Int. Ed.* **57**, 11758–11763 (2018).
27. Pang, X., Lv, J., Zhu, C., Qin, L. & Yu, Y. Photodeformable azobenzene-containing liquid crystal polymers and soft actuators. *Adv. Mater.* **31**, 1904224 (2019).

28. Sitti, M. & Wiersma, D. S. Pros and cons: Magnetic versus optical microrobots. *Adv. Mater.* **32**, 1906766 (2020).
29. Hu, Y., Li, Z., Lan, T. & Chen, W. Photoactuators for direct optical-to-mechanical energy conversion: from nanocomponent assembly to macroscopic deformation. *Adv. Mater.* **28**, 10548–10556 (2016).
30. Zeng, H., Wasylczyk, P., Wiersma, D. S. & Priimagi, A. Light robots: Bridging the gap between microrobotics and photomechanics in soft materials. *Adv. Mater.* **30**, 1703554 (2018).
31. Kuenstler, A. S., Kim, H. & Hayward, R. C. Liquid crystal elastomer waveguide actuators. *Adv. Mater.* **31**, 1901216 (2019).
32. Zhou, Y., Hauser, A. W., Bende, N. P., Kuzyk, M. G. & Hayward, R. C. Waveguiding microactuators based on a photothermally responsive nanocomposite hydrogel. *Adv. Funct. Mater.* **26**, 5447–5452 (2016).
33. Zmyslony, M. *et al.* Optical pliers: Micrometer-scale, light-driven tools grown on optical fibres. *Adv. Mater.* **32**, 2002779 (2020).
34. Yao, N. *et al.* Ultra-long subwavelength micro/nanofibres with low loss. *IEEE Photonics Technol. Lett.* **32**, 1069–1072 (2020).
35. Xu, Y., Fang, W. & Tong, L. Real-time control of micro/nanofibre waist diameter with ultrahigh accuracy and precision. *Opt. Express* **25**, 10434–10440 (2017).
36. Nagai, R. & Aoki, T. Ultra-low-loss tapered optical fibres with minimal lengths. *Opt. Express* **22**, 28427–28436 (2014).
37. Han, B., Zhang, Y. L., Chen, Q. D. & Sun, H. B. Carbon-based photothermal actuators. *Adv. Funct. Mater.* **28**, 1802235 (2018).
38. Bowden, N., Huck, W. T. S., Paul, K. E. & Whitesides, G. M. The controlled formation of ordered, sinusoidal structures by plasma oxidation of an elastomeric polymer. *Appl. Phys. Lett.* **75**, 2557–2559 (1999).
39. Birks, T. A. & Li, Y. W. The shape of fibre tapers. *J. Lightwave Technol.* **10**, 432–438 (1992).
40. Wang, P. *et al.* Single-band 2-nm-line-width plasmon resonance in a strongly coupled au nanorod. *Nano Lett.* **15**, 7581–7586 (2015).
41. Zhang, Z. *et al.* Optical micro/nanofibre embedded soft film enables multifunctional flow sensing in microfluidic chips. *Lab chip* **20**, 2572–2579 (2020).
42. Pan, J., Zhang, Z., Jiang, C., Zhang, L. & Tong, L. A multifunctional skin-like wearable optical sensor based on an optical micro-/nanofibre. *Nanoscale* **12**, 17538–17544 (2020).

Figures

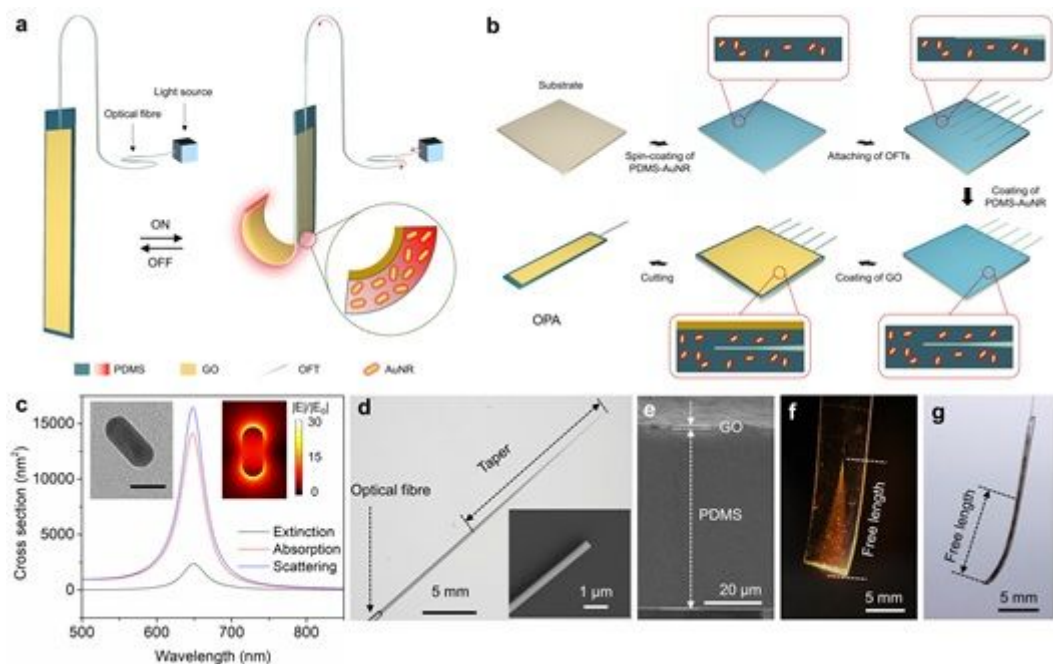


Figure 1

Structure, mechanism and fabrication of OPAs. a Schematic of the structure and driving mechanism of the OPA. b Preparation process of OPAs. c Calculated extinction, absorption and scattering cross section of an AuNR. The insets present a transmission electron microscope image of an AuNR (left) and a calculated near-field distribution of an AuNR at the wavelength of 638 nm (right). Scale bar: 30 nm. d Optical microscope image of an OFT with a taper length of ~ 1.75 cm. The inset presents a scanning electron microscopy image of the tip of the OFT showing a diameter of ~ 700 nm. e Cross-sectional view of the PDMS-GO film. The thicknesses of PDMS and GO layer are ~ 70 and 1.5 μm , respectively. f Photograph of sending 635-nm light into an OPA with a broadened width to show the light propagation path. g Photograph of an OPA with a typical size of ~ 500 μm in width and ~ 1 cm in free length.

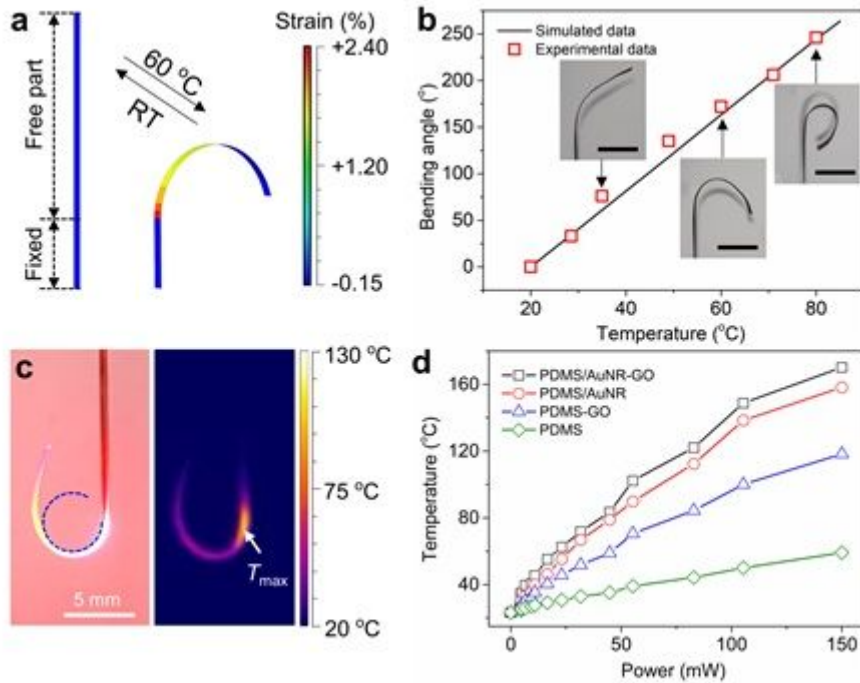


Figure 2

Deformation and photothermal heating of OPA. a Finite element analysis of the OPA model ($10 \times 0.5 \times 0.07 \text{ mm}^3$) by applying homogeneous temperature on the structure. b Simulated and experimental thermal bending angles of the OPA ($10 \times 0.5 \times 0.07 \text{ mm}^3$) under different temperature. Scale bar: 5 mm. c Photograph (left) and infrared thermography image (right) of the OPA under 635-nm laser of 75 mW. d Measured T_{max} of the OPA with various components as a function of the laser power.

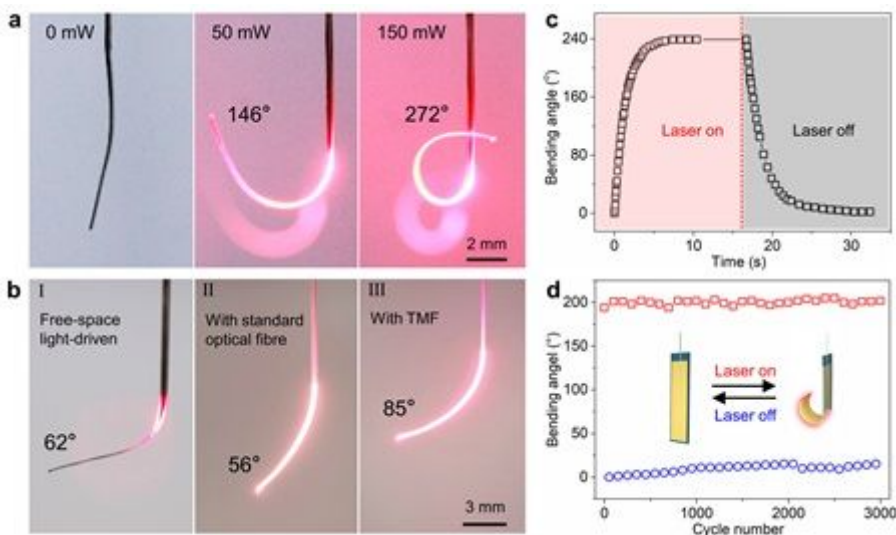


Figure 3

Light-driven actuating performances of OPA. a Photographs showing the light-driven bending of an OPA ($10 \times 0.5 \times 0.07 \text{ mm}^3$) under different laser powers. b Free-space light-driven bending of the OPA (I), waveguided light-driven bending of an actuator (thickness of $\sim 220 \text{ }\mu\text{m}$) fabricated using a standard

optical fibre (II), and waveguided light-driven bending of OPA with a thickness of $\sim 225 \mu\text{m}$ (III) under 635-nm-wavelength laser (150 mW). c Light-driven bending of an OPA (the same as in a) exposed to 635-nm-wavelength laser as a function of time. d Bending angles of the OPA over 3000 cycles of on-off switch of laser with a power of 100 mW.

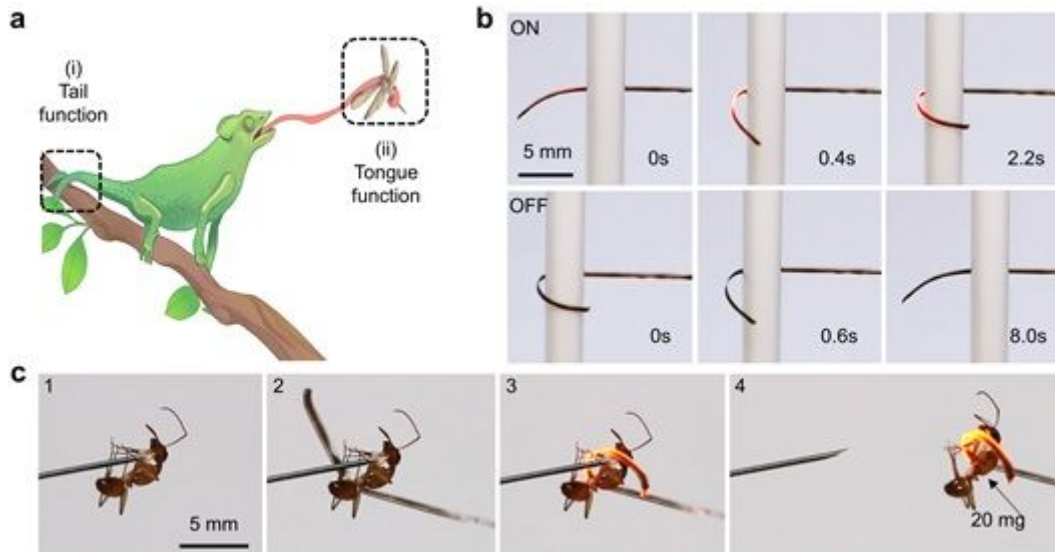


Figure 4

Biomimetic functions of OPA. a Schematic of a chameleon preying an insect. During the predation, the tail winds a branch to keep balance (i), and the tongue reaches out and captures the insect (ii). b The OPA winds and unwinds a pipe, imitating the function of the tail of a chameleon. c The OPA captures an ant, imitating the function of the tongue of a chameleon.

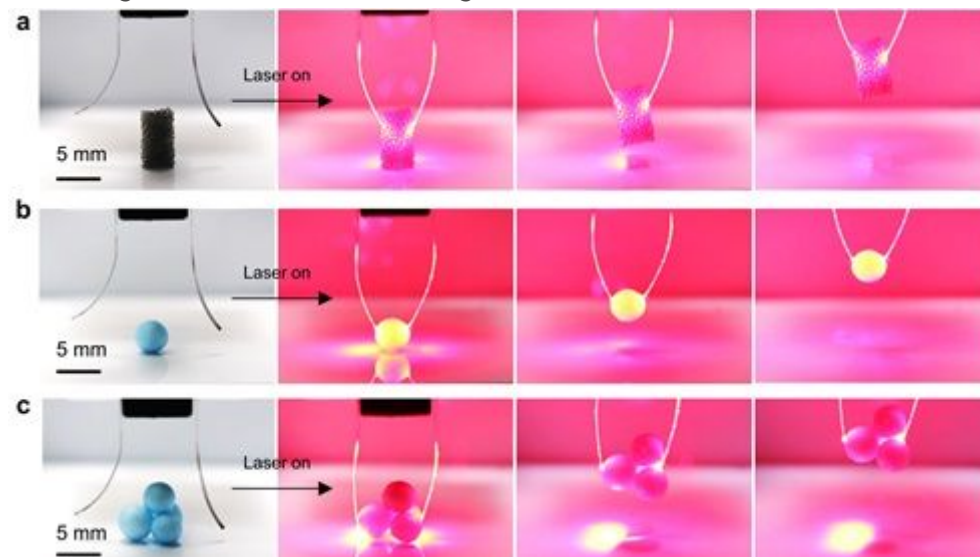


Figure 5

Two-arm OPA soft gripper for capturing objects. a The OPA soft gripper captures a small cuboid ($7 \times 3.5 \times 4 \text{ mm}^3$). b The OPA soft gripper captures a small ball (4 mm of diameter). c The OPA soft gripper captures three small balls glued together.

Supplementary Files

This is a list of supplementary files associated with this preprint. Click to download.

- [DescriptionofAdditionalSupplementaryFiles.docx](#)
- [SupplementaryMovie1.mp4](#)
- [SupplementaryMovie2.mp4](#)
- [SupplementaryMovie3.mp4](#)
- [SupplementaryMovie4.mp4](#)
- [SupplementaryMovie5.mp4](#)
- [SupplementaryMovie6.mp4](#)
- [SupplementaryMovie7.mp4](#)
- [SupplementaryMovie8.mp4](#)
- [SupplementaryInformation.docx](#)